Monthly Notices of the ROYAL ASTRONOMICAL SOCIETY

MNRAS **536,** 3431–3444 (2025) https://doi.org/10.1093/mnras/stae2768
Advance Access publication 2024 December 20

Circumbinary accretion as a diagnostic for binary–disc misalignment

Jeremy L. Smallwood [1,2★], Ya-Ping Li [3], Hongping Deng [3] and Alessia Franchini [4]

[1]*Institute of Astronomy and Astrophysics, Academia Sinica, Taipei 10617, Republic of China*
[2]*Homer L. Dodge Department of Physics and Astronomy, The University of Oklahoma, Norman, OK 73019, USA*
[3]*Shanghai Astronomical Observatory, Chinese Academy of Sciences, Shanghai 200030, People's Republic of China*
[4]*Institut für Astrophysik, Universität Zürich, Winterthurerstrasse 190, CH-8057 Zürich, Switzerland*

Accepted 2024 December 10. Received 2024 November 7; in original form 2024 August 13

ABSTRACT

Binary star systems can accrete material originating from a circumbinary disc. Since it is common for the circumbinary disc to be tilted with respect to the binary orbital plane, we test whether the accretion dynamics can be a diagnostic for binary–disc misalignment. We present hydrodynamical simulations to model the accretion flow from a circumbinary disc around an eccentric binary with initial tilts ranging from 0° to 180° in increments of 15°. Based on the initial tilt, the circumbinary disc will align towards three different configurations: prograde coplanar, polar, or retrograde coplanar. For discs with initial tilts evolving towards prograde coplanar alignment, the accretion rates on to the primary and secondary stars exhibit alternating preferential accretion. Circumbinary discs evolving towards polar alignment exhibit no alternating preferential accretion on to the binary unless the initial tilt is close to the critical tilt that sets the boundary between coplanar or polar alignment. Such cases cause strong disc warping, leading to disc breaking. The inner disc becomes eccentric, leading to alternating preferential accretion on to the binary. As the break propagates outward, the disc tilt damps towards a polar state and the disc eccentricity decreases. As the disc recircularizes, the accretion rate transitions back from alternating preferential accretion to non-alternating accretion. Lastly, no alternating preferential accretion exists for discs undergoing retrograde coplanar alignment. From the summary of the accretion rates from our suite of smoothed particle hydrodynamics simulations, it is evident that the accretion rate evolution can be affected by the initial tilt and subsequent evolution of the circumbinary disc.

Key words: accretion, accretion discs – hydrodynamics – binaries: general.

1 INTRODUCTION

The orbital evolution of a binary system can be strongly influenced by the interaction between the binary components and the surrounding gas (Bate, Bonnell & Bromm 2002). The gas settles in a circumbinary disc and the binary torque carves a wide cavity in the disc, possibly limiting the process of accretion (Artymowicz & Lubow 1994). Artymowicz & Lubow (1996) demonstrated, using 3D hydrodynamical simulations that the gas can leak into the cavity through high-speed streams originating along the outside of the cavity and spiraling inward to the central binary. The dynamics of these streams and the subsequent formation of circumstellar discs has been investigated in detail using more modern simulations (Shi et al. 2012; D'Orazio, Haiman & MacFadyen 2013; Miranda, Muñoz & Lai 2017).

The binary can exchange angular momentum and energy with the surrounding disc via accretion and gravitational torques (Roedig et al. 2012; Farris et al. 2014) and this translates into an evolution of its orbital parameters: eccentricity and semimajor axis. The evolution of both parameters has been investigated recently by a number of works, using both 2D fixed binary orbit simulations (Muñoz, Miranda & Lai 2019; Duffell et al. 2020; Muñoz & Lithwick 2020; Tiede et al. 2020) and 3D live binary simulations with isothermal discs (Ragusa, Lodato & Price 2016; Heath & Nixon 2020; Franchini, Lupi & Sesana 2022; Franchini et al. 2023) and massive self-gravitating discs (Roedig et al. 2012; Franchini, Sesana & Dotti 2021; Franchini et al. 2024). The vast majority of these simulations are scale free so their results can in principle be applied to both the massive black hole binary regime and the binary star case. We here consider the latter.

The mass accretion rate on to each star, $\dot{M}_{\rm acc}$, is instrumental for the study of the accretion disc evolution. Observationally, $\dot{M}_{\rm acc}$ can be estimated by measuring the flux of continuum and line emissions resulting from the shock of infalling gas from a disc on to the central star along the stellar magnetic field lines (e.g. Calvet & Gullbring 1998). Observations reveal accretion rates on to binary star systems are comparable to that of accretion rates on to single T Tauri stars (White & Ghez 2001), which are typically in the range of $\sim 10^{-10} - 10^{-7}\,{\rm M}_{\odot}\,{\rm yr}^{-1}$ (Valenti, Basri & Johns 1993; Gullbring et al. 1998; Calvet et al. 2004; Ingleby et al. 2013). Furthermore, observations of binary star systems suggest that the more massive star typically exhibits a higher accretion rate compared to the less massive one (White & Ghez 2001). Additionally, Manara et al. (2012) noted an increase in $\dot{M}_{\rm acc}$ with stellar mass, which decreases over evolutionary time, based on observations of the Orion Nebula Cluster.

★ E-mail: drjeremysmallwood@gmail.com

Variations in the circumbinary gas disc and gas streams structure depend significantly on binary eccentricity and mass ratio (Siwek et al. 2023). High-eccentricity binaries with mass ratios close to unity exhibit notable accretion rate modulations, occurring on time-scales similar to the binary orbital period ($P_{\rm orb}$), driven by time-varying gravitational forces. Additionally, these binaries lead to substantial eccentricity in the circumbinary disc eventually dissipating and reaching a steady value of ~ 0.3 (e.g. Lubow & Artymowicz 2000; Papaloizou, Nelson & Masset 2001; MacFadyen & Milosavljević 2008; Cuadra et al. 2009; D'Orazio et al. 2013; Muñoz & Lai 2016; Miranda et al. 2017; Thun, Kley & Picogna 2017; Muñoz et al. 2019; Muñoz & Lithwick 2020; Duffell et al. 2024). Therefore, the eccentric circumbinary disc's apsidal precession around such binaries results in preferential alternating accretion of material between the binary members over time (Muñoz & Lai 2016). On the contrary, circular equal-mass binaries do typically exhibit accretion rate modulations on both the binary orbital period and on the time-scale related to the disc inner edge orbital motion, i.e. $5\,P_{\rm orb}$ (Franchini et al. 2023; Lai & Muñoz 2023).

The preferential alternating accretion phenomenon can explain why such observations, like the eccentric T Tauri binary TWA 3A, shows a dominant accretion on to the primary (Tofflemire, Mathieu & Johns-Krull 2019), while most simulations suggest that the accretion on to secondary is preferred (Bate et al. 2000; Farris et al. 2014; Muñoz et al. 2020). Dunhill, Cuadra & Dougados (2015) modelled a coplanar circumbinary disc around the eccentric binary HD 104 237 and found the accretion rate on to the binary results in a periodic accretion variability. Furthermore, Ragusa et al. (2020) found similar eccentric behaviour in coplanar circumbinary discs around a circular binary utilizing 3D hydrodynamical simulations.

Early hydrodynamics simulations conducted by Bate & Bonnell (1997) and Bate et al. (2000) revealed that the secondary star can manifest a significantly higher accretion rate than the primary under conditions where the gas possesses substantial angular momentum. This phenomenon is thought to occur because the secondary star occupies a larger orbit and thus orbits closer to the inner edge of the disc, facilitating greater gas accretion. Nevertheless, if this were universally true, the binary mass ratio would trend towards unity (Hanawa, Ochi & Ando 2010), yet observations indicate the prevalence of unequal-mass binaries (Duquennoy & Mayor 1991). Contradictorily, grid-based simulations by Ochi, Sugimoto & Hanawa (2005) indicated a higher accretion rate for the primary star. Furthermore, Hanawa et al. (2010) computed gas accretion from a circumbinary disc utilizing a more precise scheme to resolve the centrifugal balance of a gas disc against gravity. Their findings suggested that the mass accretion rate typically favours the primary star. Preferential accretion on to one of the binary component has been the subject of more recent studies (Duffell et al. 2020; Siwek et al. 2023; Franchini et al. 2024) that presented similar results in terms of its dependence on the initial binary mass ratio. In particular, these studies confirm the preferential accretion on to the secondary star as long as the binary eccentricity is < 0.8 and the mass ratio is < 0.3. In their study, Ceppi et al. (2022) performed smoothed-particle hydrodynamical simulations of hierarchical triple star systems, focusing on the accretion rates within a coplanar circumtriple disc. Their results indicate that if the inner binary's mass exceeds that of the tertiary component, the typical differential accretion process, in which the secondary star accretes more material, is impeded. However, when the inner binary is less massive than the third body, this differential accretion scenario is enhanced.

There is little known about the accretion evolution on to binaries from misaligned circumbinary discs. Recently, Smallwood, Lubow & Martin (2022) analysed the accretion of material from a polar circumbinary. They found that the binary does not excite significant eccentricity in the disc, resulting in no alternating preferential accretion. This is because tidal torques due to Lindblad resonances on a polar circumbinary disc approach zero in the limit of unity binary eccentricity (Lubow & Martin 2018). In this work, we use hydrodynamical simulations to model circumbinary discs with misalignments with respect to the binary orbital plane in the range $0^\circ - 180^\circ$ in steps of 15° and track the accretion evolution on to the binary. At a given radius, tidal torques are weaker for a misaligned circumbinary disc, giving rise to smaller central cavities (Lubow, Martin & Nixon 2015; Miranda & Lai 2015; Franchini, Lubow & Martin 2019), which may impact the accretion dynamics. We find that the accretion pattern may be used to infer the binary–disc misalignment.

The structure of the paper is as follows: We detail the initial setup of the hydrodynamical simulation in Section 2. We present the results in Section 3 and give a discussion in Section 4. Finally, we draw our conclusions in Section 5.

2 METHODS

2.1 Binary and disc setup

To model the accretion of material from misaligned circumbinary discs, we use the smoothed particle hydrodynamical code PHANTOM (Price et al. 2018).PHANTOM has been successful in modelling misaligned circumbinary discs (e.g. Nixon 2012; Nixon, King & Price 2013; Doğan et al. 2015; Facchini, Juhász & Lodato 2018; Aly & Lodato 2020; Smallwood et al. 2020, 2022). The discs within our hydro model are in the bending wave regime, meaning that the disc aspect ratio, H/r, is larger than the Shakura & Sunyaev (1973) α-viscosity parameter, which is appropriate for protoplanetary discs (e.g. Hueso & Guillot 2005; Rafikov 2016; Ansdell et al. 2018). In this regime, warps induced in the disc by the binary torque propagate as bending waves with a vertical averaged speed $c_{\rm s}/2$ (Papaloizou & Lin 1995), where $c_{\rm s}$ is the sound speed.

We setup an equal-mass eccentric binary with a semimajor axis $a = 1$ and initial eccentricity $e_{\rm b} = 0.5$. The binary separation and eccentricity are allowed to evolve in time. We employ a Cartesian coordinate system (x, y, z), where the x-axis aligns with the direction of the binary eccentricity vector, and the z-axis aligns with the direction of the binary angular momentum vector. We model the equal-mass binary as a pair of sink particles with a total mass $M_1 + M_2 = M$, where M_1 and M_2 are the masses of the primary and secondary binary components, respectively. The binary accretion radii are set to $r_{\rm acc,1} = r_{\rm acc,2} = 0.25a$. The sink accretion radius is considered a hard boundary, where the accreted particles' mass and angular momentum are added to the sink (Bate, Bonnell & Price 1995). Smallwood et al. (2022) performed a resolution study about how the accretion radii affect the accretion rate. They found that the accretion rate with the smallest accretion radius, $0.01a$ (comparable to the size of the star), was similar to the accretion rate for $r_{\rm acc} = 0.25a$. We therefore chose a larger sink radius in order to decrease the computational time.

The circumbinary disc is modelled with initially 1×10^6 equal-mass smoothed particle hydrodynamics (SPH) particles with a total disc mass $M_{\rm d} = 10^{-3}$ M. The particles are radially distributed from the inner disc radius, $r_{\rm in} = 4a$, to the outer disc radius, $r_{\rm out} = 7a$. A coplanar disc around a binary would have an inner truncation radius of about $3a$ (Artymowicz & Lubow 1994), whereas a tilted circumbinary disc can radially extend much closer to the binary orbit

due to the weaker binary gravitational torque experienced by the off-plane material. The observations of the polar disc around HD 98800 BaBb reveal indeed an inner disc radius of $\sim 1.6a$ (Franchini et al. 2019). The chosen value of $r_{\rm in} = 4a$ exceeds the tidal truncation limit for both extremes: coplanar and polar configurations. This allows the material to initially viscously drift inward down to the effective truncation radius before the disc settles into a quasi-steady state (e.g. Smallwood et al. 2022). A smaller initial disc inner edge would only cause an initial transient in the accretion rate on to the binary as the mass within the truncation radius is quickly accreted (e.g. Smallwood et al. 2021a). This transient would furthermore cause the resolution of the simulations to decrease as the disc loses mass. We find the long-term accretion rate from a coplanar disc starting at $2a$ or at $4a$ to be the same. Additionally, the disc mass is not large enough for self-gravity to be important.

The gas surface density profile is initially a power-law distribution given by

$$\Sigma(r) = \Sigma_0 \left(\frac{r}{r_{\rm in}}\right)^{-p}, \tag{1}$$

where $\Sigma_0 = 6.75 \times 10^{-10}\,{\rm M\,a^{-2}}$ is the density normalization (defined by the total mass), p is the power-law index, and r is the spherical radius. We set $p = 3/2$. We adopt the locally isothermal equation of state of Farris et al. (2014) and set the sound speed c_s to be

$$c_{\rm s} = c_{\rm s0} \left(\frac{a_{\rm b}}{M_1 + M_2}\right)^q \left(\frac{M_1}{R_1} + \frac{M_2}{R_2}\right)^q, \tag{2}$$

where R_1 and R_2 are the radial distances from the primary and secondary star, respectively, and $c_{\rm s0}$ is a constant with dimensions of velocity This approach to the sound speed distribution ensures that the temperatures around the circumprimary and circumsecondary discs are primarily influenced by the irradiation from the primary and secondary stars, respectively. For $R_1(R_2) \gg a$, the sound speed is set by the distance from the binary centre of mass. The disc thickness is scaled with radius as

$$H = \frac{c_{\rm s}}{\Omega} \propto r^{3/2-q}, \tag{3}$$

where $\Omega = \sqrt{GM/r^3}$ and $q = 3/4$. We set an initial gas disc aspect ratio of $H/r = 0.1$ at $r = r_{\rm in}$. The Shakura & Sunyaev (1973) viscosity, $\alpha_{\rm SS}$, prescription is given by

$$\nu = \alpha_{\rm SS} c_{\rm s} H, \tag{4}$$

where ν is the kinematic viscosity. In order to simulate $\alpha_{\rm SS}$, we use the artificial viscosity $\alpha^{\rm av}$ prescription in Lodato & Price (2010) given as

$$\alpha_{\rm SS} \approx \frac{\alpha_{\rm AV}}{10} \frac{\langle h \rangle}{H}. \tag{5}$$

We take the Shakura & Sunyaev (1973) $\alpha_{\rm SS}$ parameter to be 0.01. The circumbinary disc is initially resolved with average smoothing length per scale height $\langle h \rangle / H = 0.20$. With the above prescription, $\langle h \rangle / H$ and $\alpha_{\rm SS}$ are constant over the radial extent of the disc (Lodato & Pringle 2007). Note, that $\langle h \rangle / H$ can vary due to the formation of warps in the disc (Fairbairn & Ogilvie 2021; Deng & Ogilvie 2022).

The material that flows into the cavity from the circumbinary disc, rather than being flung back to its inner edge, will ultimately be accreted on to the sinks. This occurs on a time-scale linked to the viscous time-scale within each circumstellar disc. However, this time-scale remains largely uncertain, as there are currently no reliable estimates for the viscosity parameter in these types of discs. Our chosen equation of state described in equation (2) allows for the formation of circumstellar discs around each component. However, the resolution of these circumstellar discs formed by the streams of material leaking from the circumbinary disc is quite low. Indeed in SPH simulation it is very challenging to resolve the dynamics in low-density regions, such as the cavity carved by the binary into the disc. Since the two circumstellar disc have low resolution, their viscous time-scale is artificially short, leading to rapid accretion of the circumstellar disc on to the binary component. In order to resolve the circumstellar discs in PHANTOM we would need to employ the method outlined in Smallwood, Martin & Lubow (2021b), where they artificially decrease the sound speed near each binary component. This increases the viscous time-scale in the circumstellar discs, enabling material accumulation around the binary components. However, employing this method would prohibit us from simulating over the extended time-scales necessary to model the quasi-steady state accretion rate from the circumbinary disc to the binary as the resolution of bound material on small-scales is computationally intensive. Hence, we decide to not resolve the formation of such discs in our hydrodynamical simulations. The buffering effect of circumstellar discs on accretion on to the stars is not considered, as the circumstellar discs are not simulated. Moreover, the likelihood of forming long-lived circumstellar discs decreases with increasing eccentricity of the binary components and/or decreasing binary separation due to tidal truncation (e.g. Artymowicz & Lubow 1994).

We explore several disc misalignment angles, uniformly sampled between coplanar and retrograde in increments of 15°.

2.2 Analysis

The analysis of the simulations presented in this work is focused on the connection between the disc properties and the accretion rate on to the binary components. In particular, we want to understand whether the fact that the disc is circulating, therefore aligning/counter-aligning with the binary orbital, or librating, therefore undergoing polar alignment, affects the preferential accretion on to one of the binary components. We operate within a framework defined by the instantaneous values of the binary eccentricity vector, $\boldsymbol{e}_{\rm b}$, and the angular momentum vector, $\boldsymbol{l}_{\rm b}$. This binary frame consists of three axes: $\boldsymbol{e}_{\rm b}$, $\boldsymbol{l}_{\rm b}$, and $\boldsymbol{l}_{\rm b} \times \boldsymbol{e}_{\rm b}$. We separate the disc into 300 bins in spherical radius. For discs undergoing coplanar prograde alignment, the radial grid spans from $2a$ to $10a$ and for discs undergoing coplanar retrograde or polar alignment, the radial grid spans from $1.5a$ to $10a$. Within each bin, we calculate the azimuthally averaged surface density, tilt, longitude of ascending node, and eccentricity. The tilt of an annulus in this disc at radius R relative to the instantaneous binary angular momentum is given by

$$i(R) = \cos^{-1}(\hat{\boldsymbol{l}}_{\rm b} \cdot \hat{\boldsymbol{l}}_{\rm d}(r)), \tag{6}$$

where $\hat{\boldsymbol{l}}_{\rm b}$ is the unit vector in the direction of the binary angular momentum vector and $\hat{\boldsymbol{l}}_{\rm d}(r)$ is the unit vector in the direction of the disc momentum vector. The inclination of the disc is then calculated as the density weighted average of the inclination given by

$$i = \frac{\int_{r_{\rm in}}^{r_{\rm out}} 2\pi r \Sigma(r) i(r)\,{\rm d}r}{M_{\rm tot}}, \tag{7}$$

where $\Sigma(r)$ represents the surface density at radius r, $i(r)$ denotes the inclination at radius r, and $M_{\rm tot}$ is the total mass of the disc at the specified time. Note, if the disc breaks, an average inclination without being density weighted would become meaningless. The longitude

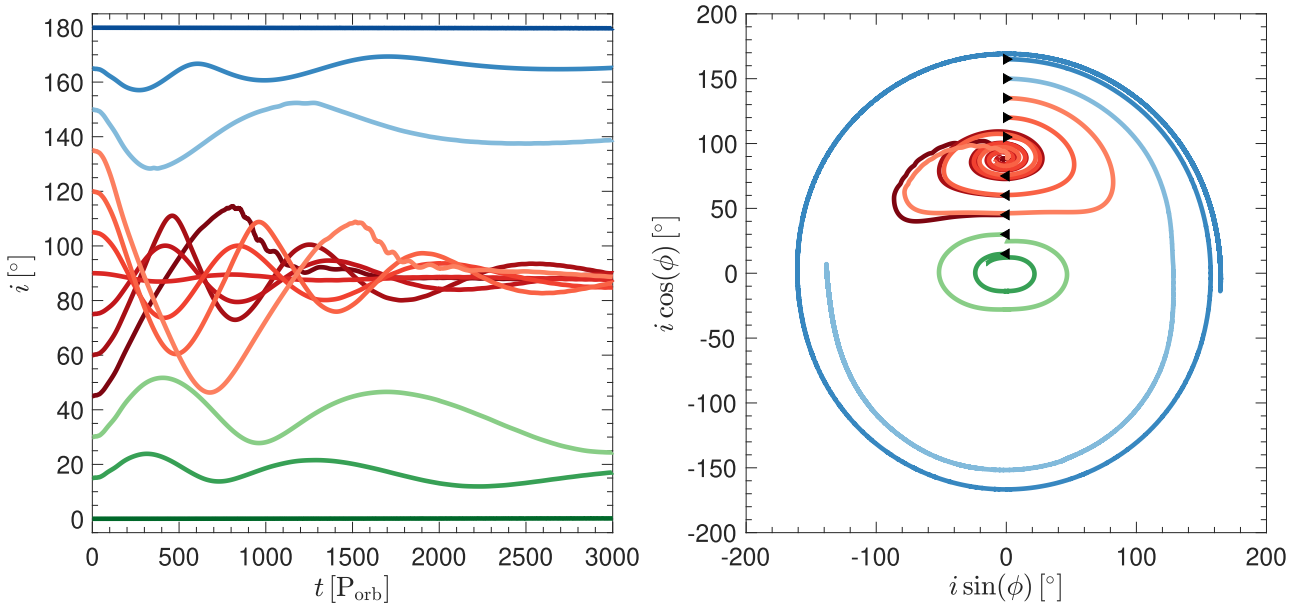

Figure 1. Left panel: the evolution of the tilt, i, as a function of time in units of initial binary orbital period, $P_{\rm orb}$. The colours denote the initial tilt of the circumbinary disc with greens evolving coplanar prograde, reds evolving polar, and blues evolving coplanar retrograde. Right panel: disc evolution in the $i\cos\phi$–$i\sin\phi$ phase space. The black triangles represent $t = 0, P_{\rm orb}$, with each triangle pointing in the direction of evolution. Note that simulations with $i_0 = 0°$, 90°, 180° are not shown because the longitude of the ascending node is undefined for coplanar disc orientations, and there is very little precession when the disc is initially polar.

of the ascending node for the disc is given by

$$\phi(r) = \tan^{-1}\left(\frac{\hat{\boldsymbol{l}}_{\rm d}(r)\cdot(\hat{\boldsymbol{l}}_{\rm b}\times\hat{\boldsymbol{e}}_{\rm b})}{\hat{\boldsymbol{l}}_{\rm d}(r)\cdot\hat{\boldsymbol{e}}_{\rm b}}\right). \tag{8}$$

Similarly, ϕ is calculated as a density weight average of the longitude of the ascending node given by

$$\phi = \frac{\int_{r_{\rm in}}^{r_{\rm out}} 2\pi r\Sigma(r)\phi(r)\,{\rm d}r}{M_{\rm tot}}. \tag{9}$$

Lastly, the disc eccentricity at radius r is calculated by

$$e(r) = \sqrt{\hat{\boldsymbol{e}}_{\rm d}(r)\cdot\hat{\boldsymbol{e}}_{\rm d}(r)}, \tag{10}$$

where $\hat{\boldsymbol{e}}_{\rm d}(r)$ is the unit vector in the direction of the disc eccentricity vector. The density weighted average of the disc eccentricity is then

$$e = \frac{\int_{r_{\rm in}}^{r_{\rm out}} 2\pi r\Sigma(r)e(r)\,{\rm d}r}{M_{\rm tot}}. \tag{11}$$

The accretion rate on to each binary component is computed directly from the simulations as the binary is live and it is allowed to accrete gas with time.

3 RESULTS

3.1 Circumbinary disc alignment

A misaligned disc around an eccentric binary can undergo circulating or librating orbits. The minimum tilt for libration is given by

$$i_{\rm min} = \arccos\left[\frac{\sqrt{5}e_{\rm b0}\sqrt{4e_{\rm b0}^2 - 4j_0^2(1-e_{\rm b0}^2)+1} - 2j_0(1-e_{\rm b0}^2)}{1+4e_{\rm b0}^2}\right] \tag{12}$$

(Martin & Lubow 2019), where $j_0 = J_{\rm d0}/J_{\rm b0}$ is the initial angular momentum ratio of the disc to the binary, and $e_{\rm b0}$ is the initial binary eccentricity. The initial angular momentum of the binary is given by

$$J_{\rm b0} = \mu\sqrt{G(M_1+M_2)a_{\rm b0}(1-e_{\rm b0}^2)}, \tag{13}$$

where μ is the reduced mass and the initial angular momentum of the disc is given by

$$J_{\rm d0} = \int_{r_{\rm in}}^{r_{\rm out}} 2\pi r^3\Sigma_0(r)\Omega{\rm d}r, \tag{14}$$

where $\Omega = \sqrt{GM/r^3}$ is the Keplerian angular velocity. For our hydro simulations, we have $j_0 \sim 0.0106$ and $e_{\rm b0} = 0.5$, which gives $i_{\rm min} \sim 38°$ or $\sim 142°$ for nodal librating orbits. Therefore, for $i_0 \lesssim 38°$ the disc will evolve to a prograde coplanarity configuration, while for $i_0 \gtrsim 142°$, the disc will evolve to a retrograde coplanarity configuration. For $38° \lesssim i_0 \lesssim 142°$, the disc will undergo nodal libration. Note that for higher binary eccentricity, the minimum inclination angle necessary for librating solutions becomes smaller.

The left panel in Fig. 1 illustrates the average disc tilt as a function of time in binary orbital periods. The different shades of green curves represent discs undergoing prograde coplanar alignment, while the different shades of blue curves denote discs undergoing retrograde coplanar alignment. The different shades of red curves depict discs undergoing polar alignment (librating orbits). In each model, tilt oscillations occur due to the torque from the eccentric binary (Smallwood et al. 2019). These oscillations dampen over time as the discs evolve closer to their respective alignment configurations. For our selected disc parameters, the polar alignment time-scale is faster than coplanar alignment. The right panel in Fig. 1 illustrates the disc evolution in the $i\cos\phi$–$i\sin\phi$ phase space. As mentioned earlier, depending on the initial disc inclination, the disc can reside on a circulating or librating orbit. The centres of the upper libration regions correspond to $i = 90°$ and $\phi = 90°$, while the centre for the lower librating region corresponds to $i = 90°$ and $\phi = -90°$. In this study, we focus on discs evolving towards the upper libration region. The distance from the centre of the circulating or librating regions

to any point on the phase diagram curve indicates the tilt of the disc. The more 'oval-shaped' the phase diagram, the larger the amplitude of the disc tilt oscillations.

The process driving alignment between the accretion disc and the binary angular momenta stems from the inherent viscosity within the disc. This viscosity effectively reduces inclination oscillations over a time-scale proportional to α^{-1}, thereby dissipating the warp (Papaloizou & Lin 1995; Lubow & Ogilvie 2000; Lubow & Martin 2018). The linear theory of warped discs describes the evolution of the warp in the regime of small inclination angles. Within the linear warp propagation theory, the warp is dissipated and the circumbinary disc aligns on a time-scale

$$\tau = \frac{1}{\alpha}\left(\frac{H}{r}\right)^2 \frac{\Omega_\mathrm{b}}{\Omega_\mathrm{d}^2}, \tag{15}$$

where α is the disc viscosity, H/r is the disc aspect ratio, and $\Omega_\mathrm{b} = \sqrt{G(M_1+M_2)/a^3}$ is the binary angular frequency. Ω_d is the global disc precession frequency, which differs depending on coplanar or polar alignment, and is given by

$$\Omega_\mathrm{d} = \begin{cases} -\frac{3}{4}\sqrt{1+3e_\mathrm{b}^2-4e_\mathrm{b}^4}\,\frac{M_1M_2}{M^2}\left\langle\left(\frac{a}{r}\right)^{7/2}\right\rangle\Omega_\mathrm{b}, & \text{coplanar,} \\ \frac{3\sqrt{5}}{4}e_\mathrm{b}\sqrt{1+4e_\mathrm{b}^2}\,\frac{M_1M_2}{M^2}\left\langle\left(\frac{a}{r}\right)^{7/2}\right\rangle\Omega_\mathrm{b}, & \text{polar} \end{cases} \tag{16}$$

(Lubow & Martin 2018; Smallwood et al. 2019), where

$$\left\langle\left(\frac{a}{r}\right)^{7/2}\right\rangle = \frac{\int_{r_\mathrm{c/p}}^{r_\mathrm{out}} \Sigma r^3\Omega(a/r)^{7/2}\,\mathrm{d}r}{\int_{r_\mathrm{c/p}}^{r_\mathrm{out}} \Sigma r^3\Omega\,\mathrm{d}r}, \tag{17}$$

and where $\Omega = \sqrt{G(M_1+M_2)/r^3}$ is the Keplerian angular frequency. The lower bound for the integrals, r_c and r_p, corresponds to the inner edge for a coplanar and polar discs, respectively. Note that if the disc breaks, the constituent discs will precess at different rates and equation (17) cannot be applied. Using equations (15) and (16), we calculate the ratio of the coplanar alignment time-scale to the polar alignment time-scale to be

$$\frac{\tau_\mathrm{c}}{\tau_\mathrm{p}} = \frac{5e_\mathrm{b}^2(1+4e_\mathrm{b}^2)}{1+3e_\mathrm{b}^2-4e_\mathrm{b}^4}\left(\frac{10-r_\mathrm{c}}{10-r_\mathrm{p}}\right)^2\left(\frac{-625r_\mathrm{p}^{5/2}+\sqrt{10}}{-625r_\mathrm{c}^{5/2}+\sqrt{10}}\right)^2\left(\frac{r_\mathrm{c}}{r_\mathrm{p}}\right)^5. \tag{18}$$

Assuming that the disc parameters (Σ, α, and H/r) are equivalent in the coplanar and polar models, $\tau_\mathrm{c}/\tau_\mathrm{p}$ is dependent on e_b, r_c, and r_p. r_c can vary with binary eccentricity, and can be estimated from Artymowicz & Lubow (1994). r_p will not vary significantly with binary eccentricity since the binary tidal torque is weaker for polar-aligning discs. We assume a constant value of $r_\mathrm{p} = 1.5a$ (Kennedy et al. 2019).

Fig. 2 shows the ratio of the coplanar alignment time-scale to the polar alignment time-scale, $\tau_\mathrm{c}/\tau_\mathrm{p}$ (from equation 18), as a function of binary eccentricity. At $e_\mathrm{b} = 0.12$, the ratio $\tau_\mathrm{c}/\tau_\mathrm{p} \approx 1$. The binary eccentricity value when $\tau_\mathrm{c}/\tau_\mathrm{p} \approx 1$ will change if the coplanar and polar discs have different disc parameters (Σ, α, and H/r) with respect to one another. Therefore, for $e_\mathrm{b} < 0.12$, the polar alignment time-scale is longer than the coplanar alignment time-scale. Conversely, for $e_\mathrm{b} > 0.12$, the polar alignment time-scale is shorter than the coplanar alignment time-scale. Given that our simulations have $e_\mathrm{b} = 0.5$, the discs aligning polar will have a shorter alignment time-scale than the simulations modelling coplanar aligning discs (see the left panel in Fig. 1). These results are in line with previous work (e.g. Li, Zhou & Zhang 2014; Miranda & Lai 2015; Martin & Lubow 2017, 2019; Cuello & Giuppone 2019; Ceppi et al. 2023).

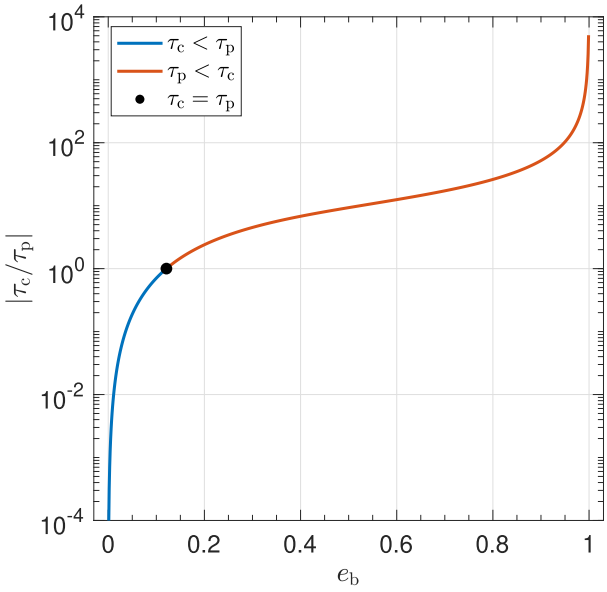

Figure 2. The ratio of the coplanar alignment time-scale to the polar alignment time-scale, $\tau_\mathrm{c}/\tau_\mathrm{p}$ (from equation 18), as a function of binary eccentricity. The blue curve represents $\tau_\mathrm{c}/\tau_\mathrm{p} < 1$ and the red curve represents $\tau_\mathrm{p}/\tau_\mathrm{c} < 1$. The black dot denotes when $\tau_\mathrm{c}/\tau_\mathrm{p} = 1$.

3.2 Circumbinary disc structure and evolution

We examine the evolution of the disc surface density and eccentricity during the disc alignment process. Fig. 3 shows the disc surface density (upper subpanel) and eccentricity (lower subpanel) as a function of time for each model. The large figure denotes the coplanar case, showing that the the surface density is smooth in radius, with the disc viscously expanding outwards. There is a small eccentricity growth that occurs within the discs due to the binary exciting eccentric modes (e.g. Lubow & Ogilvie 2000; Muñoz & Lai 2016; Muñoz et al. 2019). The inclined discs models undergoing coplanar alignment, i.e. $i_0 \leq 30°$, show similar results to the coplanar disc case. Next, we analyse the discs that are undergoing polar alignment. For $i = 45°$, the surface density profile reveals disc breaking at $r \sim 2a$. Due to the initial disc tilt being close to the critical tilt for circulation or libration, the disc becomes strongly warped, forcing the disc to break. As the disc breaks, the inner disc becomes very eccentric, reaching an azimuthally averaged eccentricity of $e \sim 0.2$. Eventually, the break dissipates as the inner and outer discs both align polar. At this point, the disc eccentricity begins to decrease. For $i_0 = 60°$, there is strong warping that occurs as the disc aligns to a polar state, but not strong enough to cause disc breaking. During the periods of strong warping, there is eccentricity growth that occurs but eventually dampens. For $i_0 = 75°$, there is very little disc warping and eccentricity growth since the initial disc tilt is close to polar. Likewise, for $i_0 = 90°$, the initially polar-aligned disc does not exhibit any strong disc warping or eccentricity growth.

Next, we examine the discs that are initially retrograde. Like the prograde models, as the initial disc tilt begins closer to the critical tilt, stronger disc warping and larger eccentricity growth occurs. This can be seen for models $i = 105°$ and $120°$ in Fig. 3, where the latter shows stronger warping and eccentricity growth but not enough to cause the disc to break. For $i_0 = 135°$ (close to the critical tilt), the disc breaks, similar to $i_0 = 45°$, but the time for the disc to break occurs much later. Once the disc is broken, the inner disc becomes very eccentric. For $i_0 = 150°$, the disc undergoes warping without breaking while

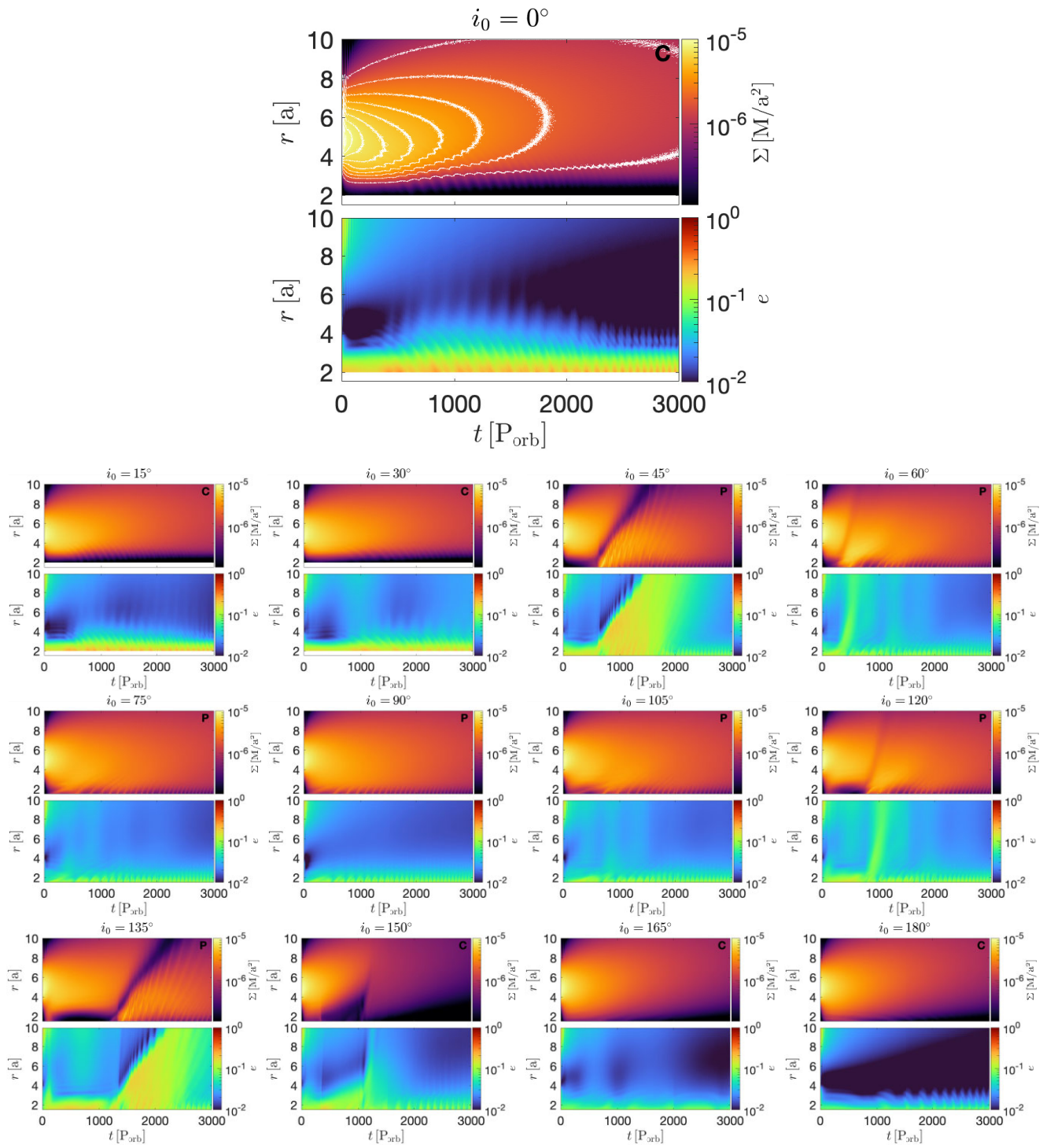

Figure 3. The disc surface density Σ (upper subpanel), and eccentricity e (lower subpanel), as a function of time in units of initial binary orbital period, $P_{\rm orb}$, for different initial misalignment of the circumbinary disc (given by the titles). We show 15 contour levels of the surface density in the enlarged panel. The letters 'C' or 'P' denote whether the disc is undergoing coplanar or polar alignment, respectively. Note that in the 45° and 135° the upper panel clearly shows a break, i.e. a discontinuity in the surface density profile.

its eccentricity increases. Lastly, for the models $i_0 = 165°$ and 180°, minimal eccentricity growth is present (especially for the $i_0 = 180°$ model). From the above analysis, we can see that the disc structure can vary depending on the initial tilt of the circumbinary disc. We investigate how the disc structure impacts the accretion rate on to the binary in Section 3.3.

We now focus on the disc structure for the two models that showed disc breaking, $i_0 = 45°$ and 135°. Fig. 4 shows the circumbinary disc structure for $i_0 = 45°$ at times ranging from $t = 0\,P_{\rm orb}$ to $t = 3000\,P_{\rm orb}$. At early times, $t < 800\,P_{\rm orb}$, the disc precesses about the eccentricity vector of the binary. At $t = 800\,P_{\rm orb}$, the disc begins to break, where the inner disc evolves quickly to a polar

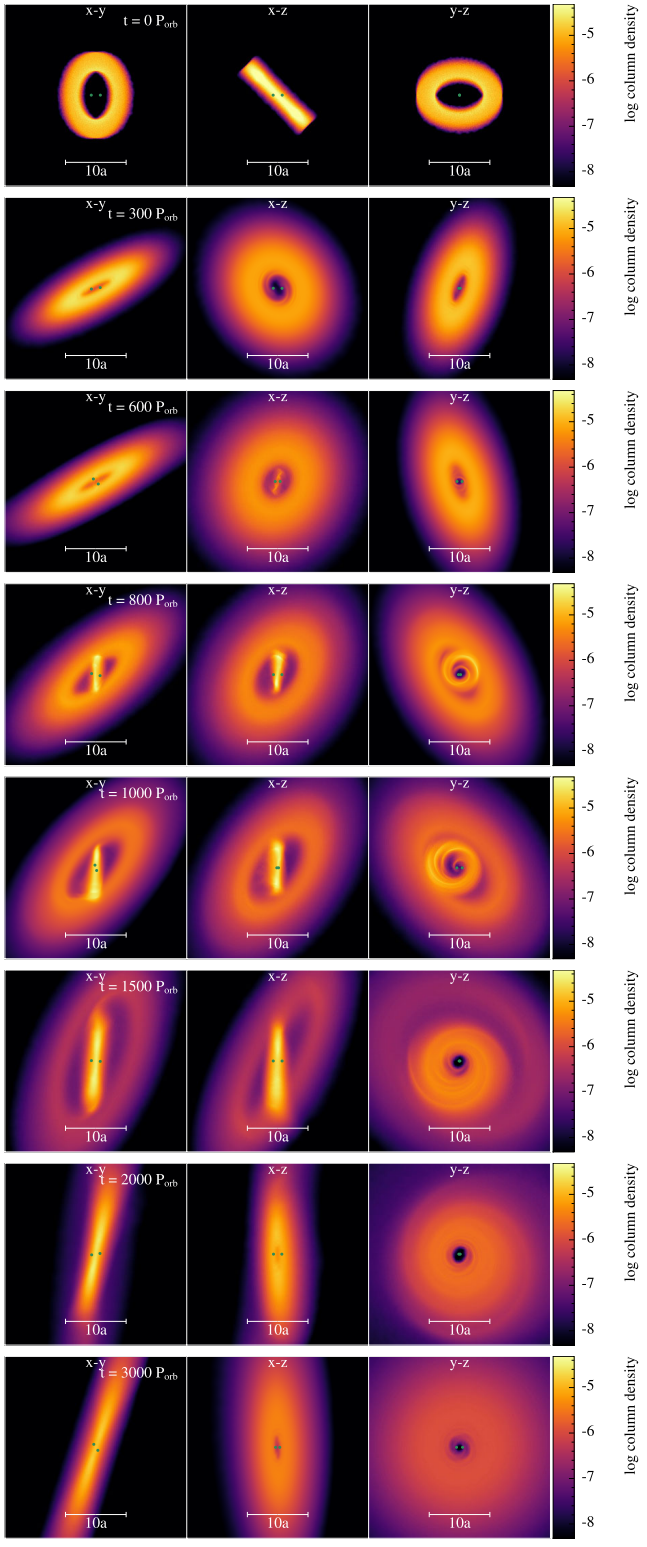

Figure 4. The gas surface density for a circumbinary disc initially misaligned by $i_0 = 45°$. The left subpanel shows the x–y plane, viewing down on the binary orbit. The middle subpanel denotes the x–z plane, which shows the initial misalignment between the disc and binary, and the right subpanel shows the y–z plane. We show selected times ranging from $t = 0\,\mathrm{P_{orb}}$ to $t = 3000\,\mathrm{P_{orb}}$, where $\mathrm{P_{orb}}$ is the initial binary orbital period.

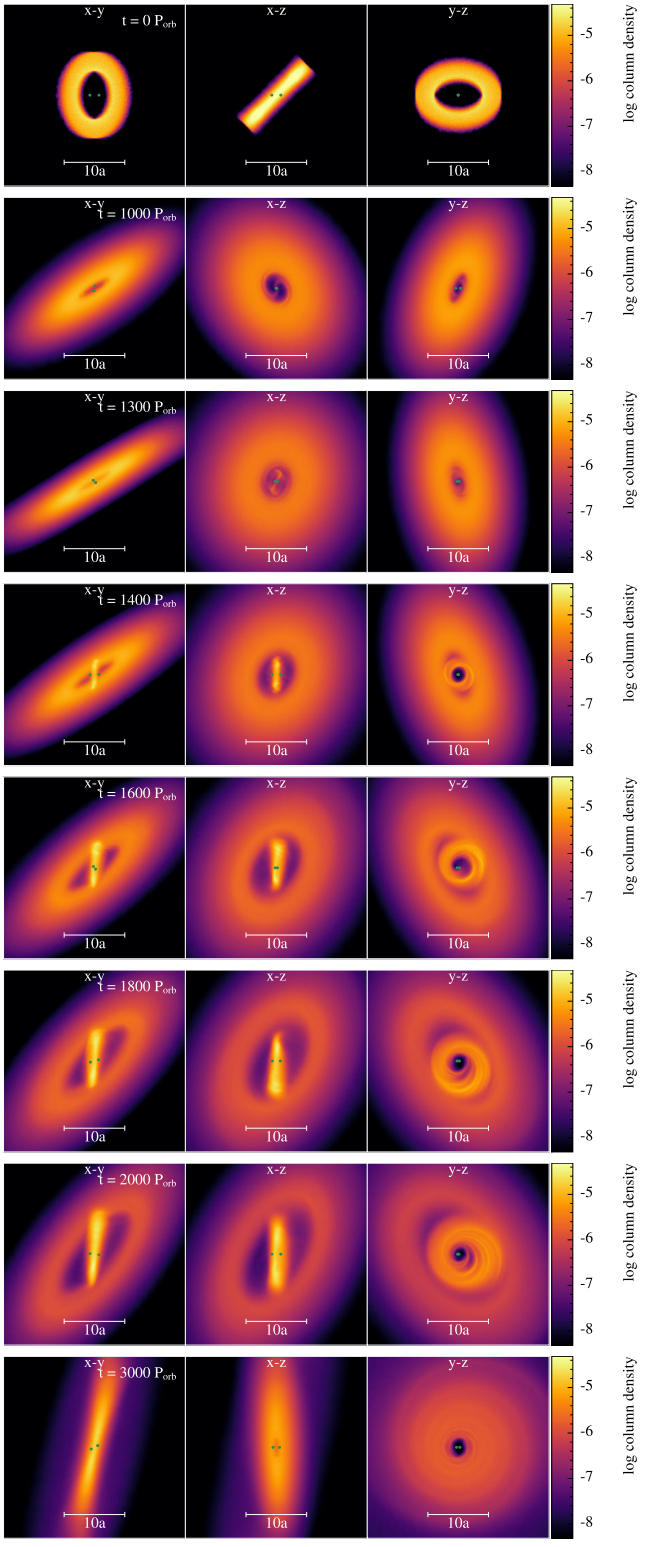

Figure 5. Same as Fig. 4, but for a initial circumbinary disc tilt of $i_0 = 135°$.

configuration, while the outer disc is still misaligned. The inner disc becomes highly eccentric and spreads outwards with time, interacting with the outer disc. Eventually, the break dissipates, and the resulting structure is a coherent polar-aligned disc (see $t = 3000\,\mathrm{P_{orb}}$). Fig. 5 shows the circumbinary disc structure for $i_0 = 135°$ at times ranging from $t = 0\,\mathrm{P_{orb}}$ to $t = 3000\,\mathrm{P_{orb}}$. At

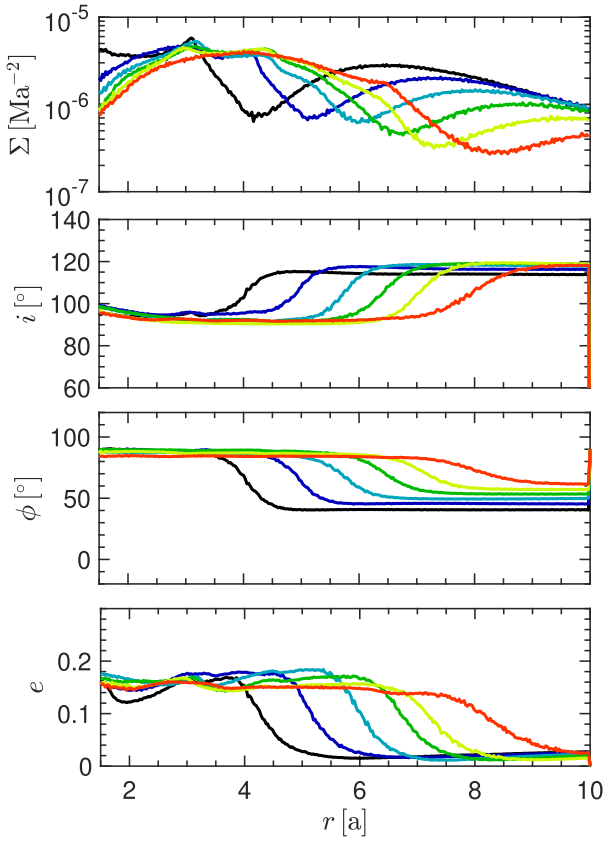

Figure 6. The evolution of the surface density, Σ, tilt, i, longitude of the ascending node, ϕ, and eccentricity, e, as a function of radius, r, for model of $i_0 = 45^\circ$ during the disc-breaking stage. We show selected times beginning with $t = 800\,\mathrm{P_{orb}}$ (black), $900\,\mathrm{P_{orb}}$ (blue), $1000\,\mathrm{P_{orb}}$ (teal), $1100\,\mathrm{P_{orb}}$ (green), $1200\,\mathrm{P_{orb}}$ (yellow), and $1300\,\mathrm{P_{orb}}$ (red). The break in the disc propagates outward as the disc aligns to a polar state.

$t < 1300\,\mathrm{P_{orb}}$, the disc precesses about the eccentricity vector of the binary with marginal warping. At $t = 1400\,\mathrm{P_{orb}}$, the disc begins to break, where the inner disc evolves quickly to a polar configuration, while the outer disc is still misaligned. The time-scale for the breaking is much longer than the $i_0 = 45^\circ$ model. The inner disc also becomes highly eccentric. As the break dissipates and the whole disc evolves to a coherent polar-aligned disc, the eccentricity begins to decrease.

We now analyse the disc break evolution for $i_0 = 45^\circ$. We note that the case for $i_0 = 135^\circ$ is qualitatively similar to the $i_0 = 45^\circ$ model. Fig. 6 shows the evolution of the surface density, tilt, longitude of the ascending node, and eccentricity as a function of radius at times $t = 800\,\mathrm{P_{orb}}$ (black), $900\,\mathrm{P_{orb}}$ (blue), $1000\,\mathrm{P_{orb}}$ (teal), $1100\,\mathrm{P_{orb}}$ (green), $1200\,\mathrm{P_{orb}}$ (yellow), and $1300\,\mathrm{P_{orb}}$ (red). At $t = 800\,\mathrm{P_{orb}}$, the break in the disc occurs at $\sim 4a$, and propagates outward with time. The inner disc aligns quickly to a polar configuration with the binary orbital plane while the outer disc is still misaligned. Similarly, the longitude of the ascending node for the inner disc is aligned to the azimuthal angle of the eccentricity vector of the binary ($\phi \sim 90^\circ$), while the outer disc is misaligned. Eventually, as the break propagates outwards, the entire disc's tilt and longitude of ascending node will be consistent with polar alignment. The inner disc is always more eccentric than the outer disc but begins to circularize with time (refer back to Fig. 3).

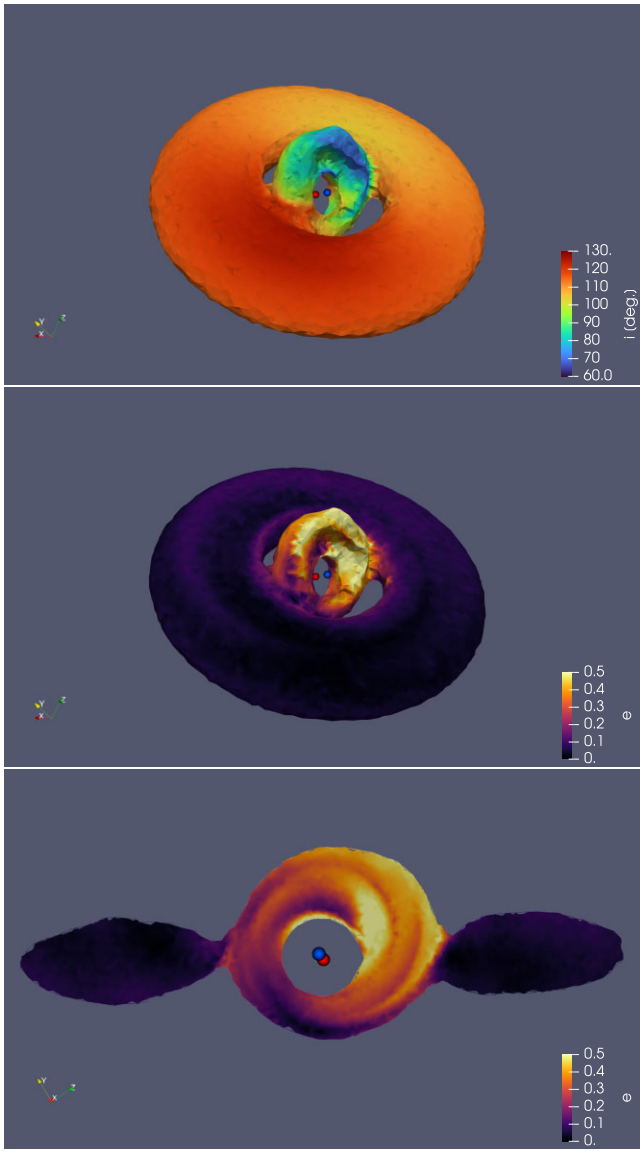

Figure 7. A 3D rendering of the circumbinary disc with $i_0 = 45^\circ$ at a time $t = 800\,P_{\mathrm{orb}}$ when the disc is breaking. The top panel shows the disc tilt with respect to the binary orbital plane. The middle panel shows the instantaneous disc eccentricity, and the bottom panel shows a cross section of the instantaneous disc eccentricity viewed face-on to the inner disc. The primary star is shown by the blue sphere, while the secondary star is denoted by the red sphere. The size of the spheres corresponds to the sink accretion radii.

Fig. 7 presents a comprehensive 3D representation of the broken disc configuration for $i_0 = 45^\circ$ during the time $t = 800, \mathrm{P_{orb}}$. The upper panel shows the tilt of the disc with respect to the binary orbital plane, the middle panel illustrates the variation of the instantaneous disc eccentricity, and the bottom panel provides a cross-sectional view of the instantaneous eccentricity distribution, with the observer viewing the inner disc face-on. We note that the inner disc is aligning polar more quickly than the outer disc. A discernible pattern emerges within the inner disc, characterized by substantial growth in eccentricity, with eccentricity values diminishing as a function of radial distance. Remarkably, the inner disc attains an instantaneous eccentricity levels reaching approximately ~ 0.5.

3.3 Accretion rate

We examine the accretion rates on to the primary and secondary stars for each SPH simulation. Fig. 8 shows a summary of the accretion rate, $\dot{M}$, on to the primary (blue) and secondary (red) stars as a function of time in binary orbital periods, P_{orb}. The accretion on to the primary and secondary stars exhibit short-term variability with time-scales similar to the binary orbital period, as expected from previous simulations of coplanar eccentric circumbinary discs (Farris et al. 2014; Duffell et al. 2020; Muñoz et al. 2020; Franchini et al. 2023; Lai & Muñoz 2023). For the disc undergoing prograde coplanar alignment, the accretion rates on to the primary and secondary exhibit antiphase behaviour. This means that when the accretion rate on to the primary is at its peak, the accretion rate on to the secondary is at its lowest. This alternating preferential accretion is present even if the circumbinary disc is tilted and aligning coplanar to the binary orbital plane. For the initial coplanar disc orientation ($i_0 = 0°$), the modulation of the alternating preferential accretion is related to the apsidal precession rate of the disc. In the limit of a coplanar pressure-less particle disc, the secular apsidal precession rate around an eccentric binary is

$$\dot{\omega}_{\rm d} \simeq \frac{3\Omega_{\rm b}}{4}\frac{q_{\rm b}}{(1+q_{\rm b})^2}\left(1+\frac{3}{2}e_{\rm b}^2\right)\left(\frac{a_{\rm b}}{r}\right)^{7/2} \tag{19}$$

(Muñoz & Lai 2016), where $q_{\rm b} = M_2/M_1$. At $r \sim 3a$, the precession period is $\sim 200\,P_{orb}$. Similar oscillations with a consistent time-scale were observed in prior works (Dunhill et al. 2015; Muñoz & Lai 2016; Muñoz et al. 2019; Lai & Muñoz 2023).

Next, we analyse the accretion rates for the disc undergoing polar alignment. The further the initial tilt of the disc is from polar, the more eccentric the disc becomes, which in turn causes oscillations in the accretion rates. If the initial tilt is close to the critical tilt for polar alignment, the large eccentricity growth causes significant fluctuations in the accretion rates, as seen in models with $i_0 = 45°$ and $i_0 = 135°$. These two models exhibit alternating preferential accretion for a period of time in a polar-aligning disc. The remaining polar-aligning models show no evidence of alternating preferential accretion; that is, the primary accretion is similar to the secondary accretion. For an initially polar disc, there are no oscillations in the accretion rates since there is little eccentricity growth present in this type of initial configuration (e.g. Smallwood et al. 2022). Lastly, we examine the accretion rates for discs undergoing retrograde coplanar alignment. These models do not show any alternating preferential accretion. However, for $i_0 = 150°$, there are oscillations in the accretion rate due to strong disc warping. From the summary of the accretion rates from our suite of SPH simulations, it is evident that the accretion rate evolution can be affected by the initial tilt of the circumbinary disc.

We further analyse the accretion rates for the two models that exhibit temporary alternating preferential accretion for a polar-aligning circumbinary disc, namely $i_0 = 45°$ and $i_0 = 135°$. Fig. 9 illustrates the accretion rate, $\dot{M}$, on to the binary from a circumbinary disc initially misaligned by $i_0 = 45°$, plotted as a function of time in binary orbital periods, P_{orb}. Prior to the disc breaking, the accretion rate displays non-alternating behaviour, with primary accretion similar to secondary accretion, as indicated by the green shaded region. Around $t = 800, P_{orb}$, the disc breaks due to the strong warping induced by the binary during polar alignment, shown by the grey shaded region. As the disc breaks, the inner disc becomes eccentric (shown in the upper panel, and also refer to Figs 3 and 7). Consequently, the accretion rate on to the binary shifts from non-alternating accretion to alternating preferential accretion, highlighted by the yellow shaded region. It is noteworthy that during this period of alternating preferential accretion, the inner disc is nearly in a polar configuration. As the disc eccentricity decreases again, the accretion rate transitions back from alternating preferential accretion to non-alternating accretion. The $i_0 = 135°$ model shows similar behaviour, as shown in Fig. 10. The main difference is that the disc breaking and period of alternating preferential accretion occurs at a later time. The accretion rate then switches back to non-alternating accretion as the disc eccentricity decreases.

4 DISCUSSION

4.1 Disc breaking

From Fig. 3, as the initial disc tilt is near the critical tilt for polar alignment, the disc breaks, causing a period of alternating preferential accretion. The break is roughly located at $4a$, which is equal to the initial inner radius of the disc in our simulations. However, disc material will flow inward, extending closer to the binary. The inner disc radius of a circumbinary disc is determined by the balance between the viscous torque exerted by the circumbinary disc and the tidal/resonant torque of the binary (Artymowicz & Lubow 1994). Under conditions of moderate orbital eccentricity, the typical inner edge resides near the 1:3 outer Lindblad resonance radius, approximately estimated to be $\sim 2a$. However, if the circumbinary disc is tilted relative to the binary orbital plane, the resonant torque weakens, resulting in a reduction of the inner disc edge (Franchini et al. 2019). When the inner radius decreases, the accumulation of material in the inner regions increases, potentially leading to a reduction in the precession time-scale compared to the radial communication time-scale, ultimately resulting in disc breaking.

The mechanism by which a warp is communicated through the disc depends on the Shakura & Sunyaev (1973) disc viscosity $\alpha_{\rm SS}$, and aspect ratio H/r. In regimes where $\alpha_{\rm SS} < H/r$, which is tipically relevant for protoplanetary discs, the warp propagates as a bending wave (Papaloizou & Lin 1995; Lubow & Ogilvie 2000). When $\alpha_{\rm SS} > H/r$, the warp propagation occurs in the diffusive regime which is applicable to thin, fully ionized discs. When warps become very large, the disc may be unable to communicate across the warp effectively. The warp may become unstable and disc breaking can occur, splitting the disc into separate rings. For our disc-breaking simulations, strong warping and a high nodal precession time-scale force the disc to break. However, predicting the location of the breaking radius is still unclear. The disc breaking phenomenon has been studied analytically (Doğan et al. 2018; Raj, Nixon & Doğan 2021) and numerically in the context of single and binary black holes (Nixon 2012; Nixon et al. 2013; Nealon, Price & Nixon 2015). Disc breaking may also be an explanation for observed disc geometries and accretion kinematics (Casassus et al. 2015; Facchini et al. 2018; Zhu 2019; Kraus et al. 2020; Nealon et al. 2022). Disc breaking is more likely for discs with smaller inner cavities, cooler temperatures, and steeper power-law profiles (e.g. Rabago et al. 2023). Analytical criterion for disc breaking has been shown by Doğan et al. (2018) and (Deng & Ogilvie 2022).

Viscosity can play a significant role in the conditions for disc breaking to occur (e.g. Drewes & Nixon 2021; Deng & Ogilvie 2022; Rabago et al. 2023; Young et al. 2023). Young et al. (2023) modelled warping and disc breaking around binary systems, finding the breaking can occur for a misalignment of $\lesssim 40°$ for moderate binary eccentricities in the bending-wave regime. For high-binary eccentricities, ~ 0.8, they found the disc is more susceptible to

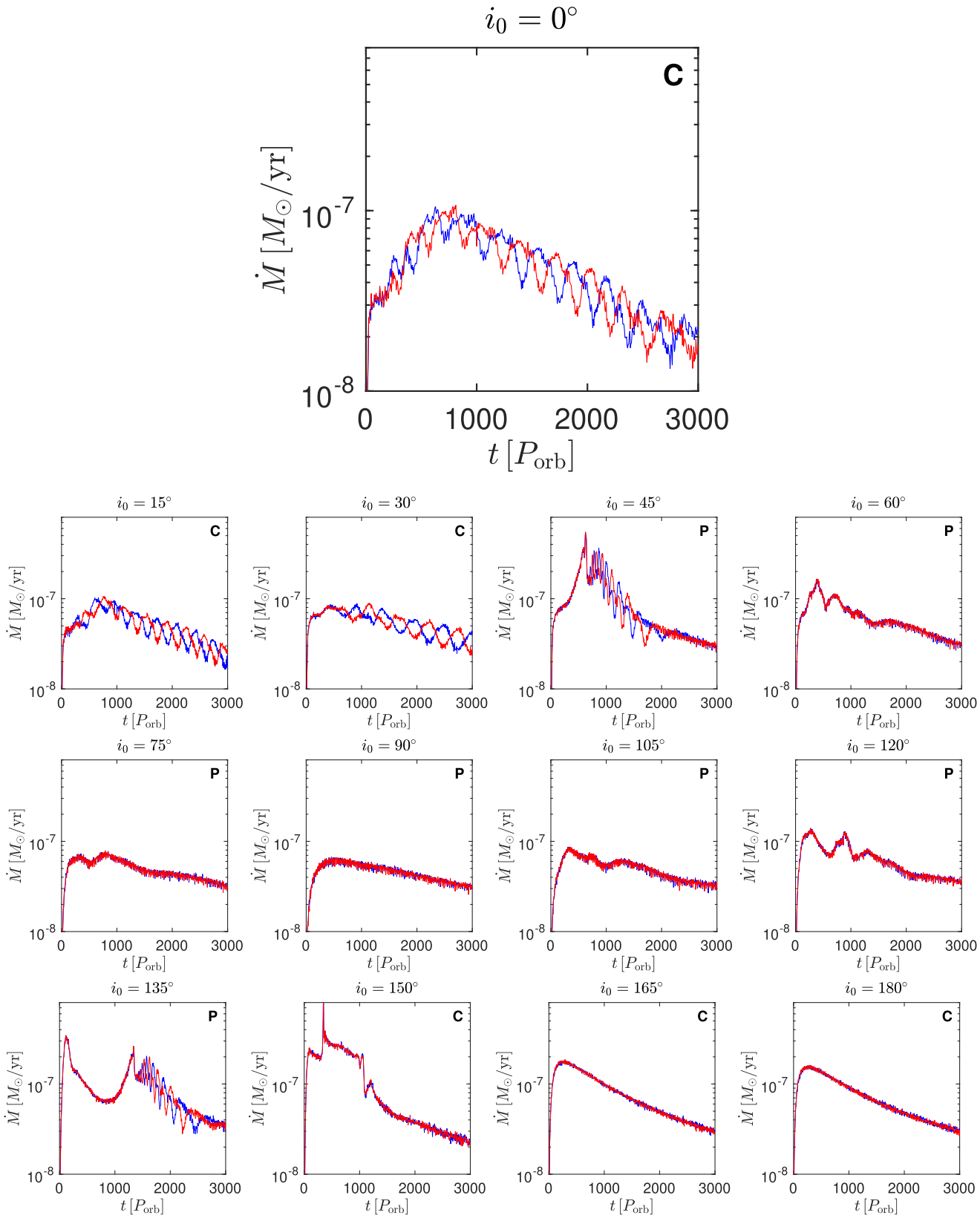

Figure 8. The accretion rate, $\dot{M}$, as a function of time in units of binary orbital period, P_orb, for different initial misalignment of the circumbinary disc (given by the titles). The blue curves represent the primary accretion, while the red curves denote the secondary accretion. The letters 'C' or 'P' denote whether the disc is undergoing coplanar or polar alignment, respectively.

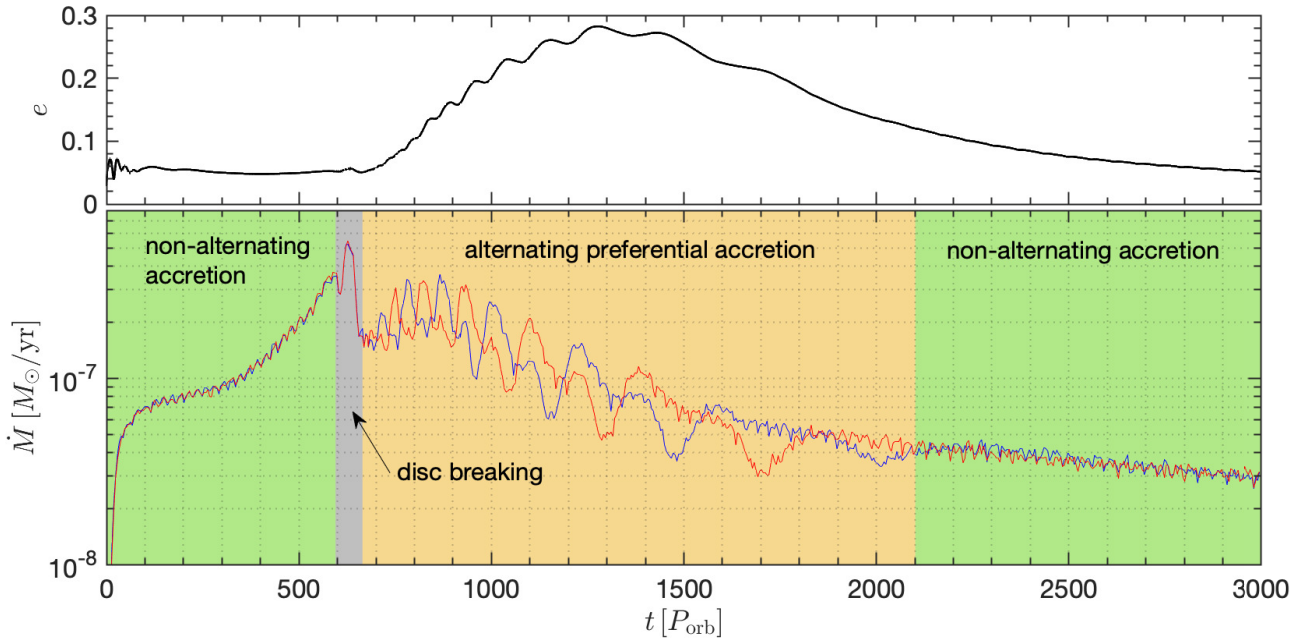

Figure 9. Upper panel: the density-weighted average disc eccentricity as a function of time in binary orbital periods, P_{orb}. Lower panel: the accretion rate, $\dot{M}$, on to a binary from a circumbinary disc initially misaligned by $i_0 = 45^\circ$ with respect to the binary orbital plane as function of time in binary orbital periods, P_{orb}. The green shaded regions denoted when the binary is undergoing non-alternating accretion, where the primary accretion (blue) and secondary accretion (red) are similar. The grey shaded regions represents the time when the disc breaks as it aligns in a polar configuration. The yellow shaded regions shows the time when the binary is undergoing alternating preferential accretion as a result of the disc breaking.

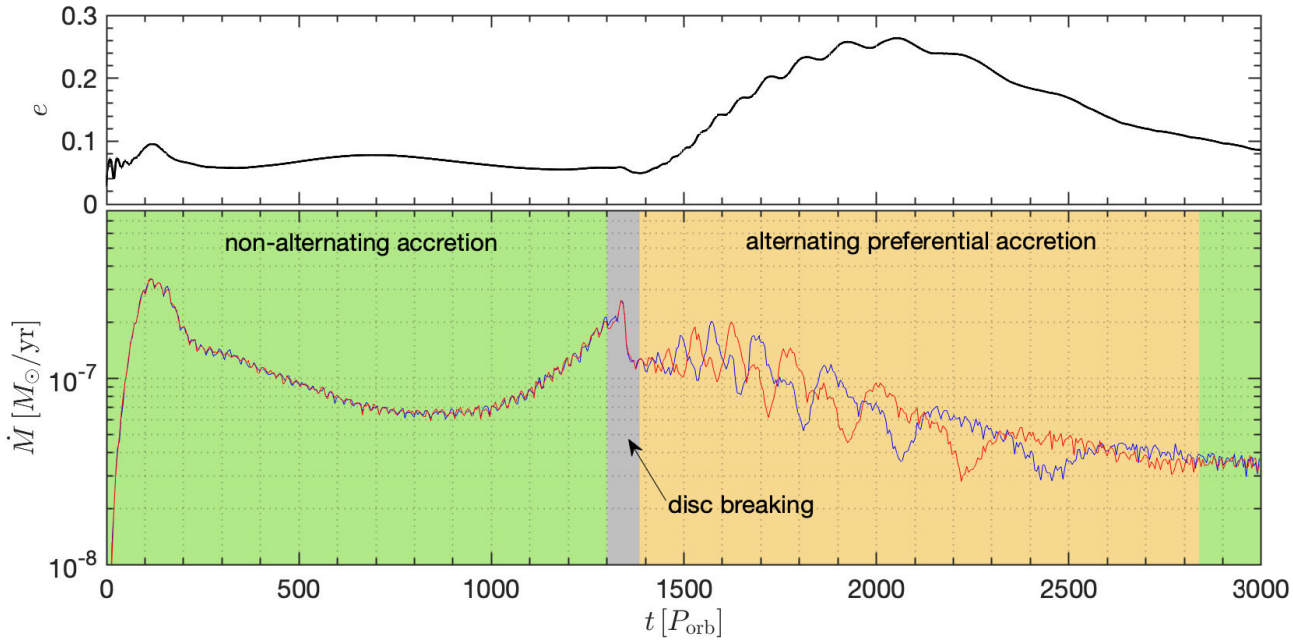

Figure 10. Same as Fig. 9, but for a initial circumbinary disc tilt of $i_0 = 135^\circ$.

breaking for lower misalignment angles. Deng & Ogilvie (2022) found that the disc broke at much smaller misalignment angle ($\sim 14^\circ$), which can be attributed to their simulated disc viscosity, as they modelled an 'inviscid' disc. In the current study, we model slightly viscous discs, similar to Young et al. (2023). However, if we model lower viscosities, approaching the inviscid regime, it may be possible that the strongly warped models in our suite of SPH simulations that did not break, will break–leading to temporary periods of alternating preferential accretion.

4.2 Resolution

The SPH method is predominantly utilized in simulations of misaligned circumbinary discs. This method incorporates explicit

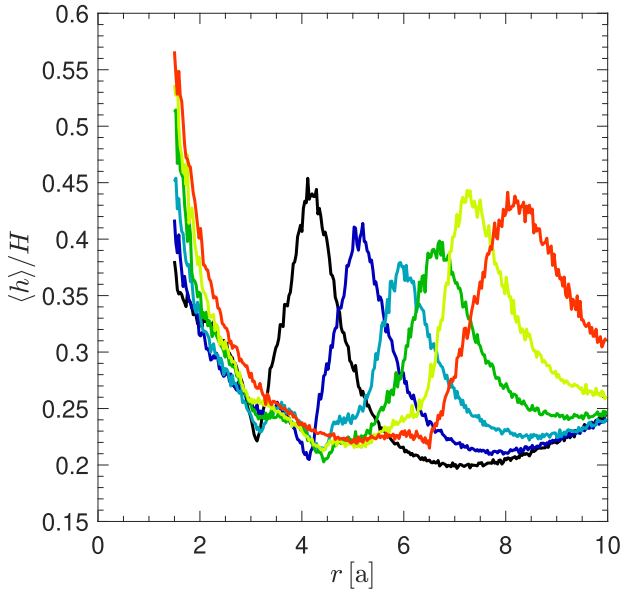

Figure 11. The average smoothing length per scale height, $\langle h \rangle / H$, as a function of disc radius, r for model of $i_0 = 45^\circ$. We show selected times beginning with $t = 800\,\mathrm{P_{orb}}$ (black), $900\,\mathrm{P_{orb}}$ (blue), $1000\,\mathrm{P_{orb}}$ (teal), $1100\,\mathrm{P_{orb}}$ (green), $1200\,\mathrm{P_{orb}}$ (yellow), and $1300\,\mathrm{P_{orb}}$ (red). The peak in the resolution is located at the breaking radius.

artificial viscosity, which, particularly at lower resolutions, may lead to a significant effective viscosity. Therefore, sufficient resolution is needed to accurately model a wave-like disc (e.g. Drewes & Nixon 2021). Drewes & Nixon (2021) illustrated that when employing sufficiently high resolution, the numerical viscosity remains low enough to attain reasonable agreement between the outcomes of PHANTOM SPH simulations in the linear regime and the linearized wave-like warp evolution equations proposed by Lubow & Ogilvie (2000).

Fig. 11 depicts the average smoothing length per scale height, $\langle h \rangle / H$, as a function of disc radius, r. We present the same times as in Fig. 6, corresponding to when the disc is broken. Smaller $\langle h \rangle / H$ means higher resolution, while larger $\langle h \rangle / H$ means lower resolution. The peaks in resolution coincide with the location of the breaking radius. The inner and outer discs are consistently well-resolved. However, the resolution worsens closer to the cavity. At the breaking radius, the resolution is $\langle h \rangle / H < 0.5$, indicating moderate resolution at the breaking radius. The magnitude of the accretion rates analysed in Fig. 8 depends on resolution. For example, for lower resolution, $\langle h \rangle / H$ may be above unity which will increase the artificial viscosity and thus artificially increase the accretion rates. This effect can be seen in Fig. 6 in Smallwood, Martin & Lubow (2023), where the lower resolution simulation has slightly higher accretion rate than the higher resolution simulation. At smaller radii in Fig. 11, the disc becomes increasingly unresolved, suggesting that the gaseous streams accreting on to the binary components are not well resolved. However, it is important to note that the focus of this work is on the accretion rate pattern and its evolution, rather than on the absolute values of the accretion rates. Therefore our results on preferential accretion alternation are not affected by the low resolution we have in the breaking discs cases.

4.3 Observational implications

Spectroscopy is one of the primary tools used to study accretion in binary systems. The VLT X-shooter spectrograph is an excellent instrument for measuring accretion rates in binary star systems, thanks to its broad wavelength coverage from ultraviolet (UV) to near-infrared (300–2500 nm) (Vernet et al. 2011). This range enables the simultaneous observation of key accretion indicators, such as H α, Ca II infrared triplet, and Br γ emission lines, which trace ionized gas accreting on to the stars (Hartmann et al. 1998). Additionally, X-shooter's capability to detect UV excess, particularly in the Balmer continuum, allows for the determination of accretion luminosity, a crucial step in calculating accretion rates (Rigliaco et al. 2012). In binary systems, where the spectra of two stars may overlap, X-shooter's high-spectral resolution enables the decomposition of individual stellar components, allowing for precise measurements of accretion rates for each star in the system (Alcalá et al. 2014; Manara et al. 2016, 2017). This multiwavelength approach is particularly effective in understanding complex accretion dynamics in young stellar systems.

Accretion rates variability can also be probed using photometric monitoring (e.g. Jensen et al. 2007). Changes in brightness, often in the UV or optical bands, are linked to accretion hotspots on the stellar surface, which form where gas from the disc impacts the star. These hotspots increase in brightness as the accretion rate intensifies, causing periodic or irregular variability in the light curves (Cody & Hillenbrand 2010; Kurosawa & Romanova 2013; Venuti et al. 2014). In binary systems, this variability can also be modulated by the orbital motion. For example, the low-mass, pre-main-sequence eclipsing binary 2M1222–57 exhibits active accretion, as evidenced by modulated H α emission (Stassun et al. 2022). While observations indicate a dominant period of P_b, simulations of a nearly circular, equal-mass ratio binary predict a dominant period of $5P_\mathrm{b}$. This discrepancy suggests that the unequal mass ratio in 2M1222–57 plays a significant role (see section 5.3 in Stassun et al. 2022). The dominant variability of 5 P_b is associated to the disc inner edge motion, which is where the accretion streams originate from (Muñoz & Lai 2016).

An example of a system that may show evidence of alternating preferential accretion is TWA 3. The TWA 3 system consists of three pre-main-sequence stars (10 ± 3 Myr, Bell, Mamajek & Naylor 2015) in a hierarchical configuration. The inner binary, TWA 3A, has an orbital period of $P = 34.8785 \pm 0.0009$ d, an eccentricity of $e = 0.628 \pm 0.006$ and a binary mass ratio of $q = 0.841 \pm 0.014$. Based on time-series photometry and high-resolution optical spectroscopy, Tofflemire et al. (2019) found the circumbinary accretion on to the TWA 3A peaks during periastron passages and shows evidence of preferential accretion on to the primary star, TWA 3Aa. However, preferential accretion switching back to the secondary is not yet currently observed. Due to the short period of the binary orbit, we may be able to observe the long-term preferential accretion behaviour within a reasonable time-scale in the future. More recently, it was found by Czekala et al. (2021) that the circumbinary disc around TWA 3A is in a nearly coplanar configuration with a tilt $< 6^\circ$ with respect to the binary orbital plane. This is consistent with our hydrodynamical simulations that a lowly inclined circumbinary disc undergoing coplanar alignment will exhibit preferential accretion on to the primary for a period of time.

High-angular-resolution techniques such as interferometry have become crucial for resolving the structures of accretion discs. Instruments like the Very Large Telescope Interferometer (VLTI)

and Atacama Large Millimeter/submillimeter Array (ALMA) can spatially resolve the circumbinary and circumstellar discs (Kraus et al. 2017; Kennedy et al. 2019; Corporaal et al. 2021). These observations allow for direct imaging the gas dynamics and disc structures, providing insight into how material is funnelled toward one or both stars (Alves et al. 2019). For example, Bohn et al. (2022) used a combination of VLTI and ALMA observations to study the misalignments in transitions discs. Such observations may be applied to understanding binary systems, as they can provide insights into how accretion flows behave in systems where the disc is not coplanar with the binary orbit, like the systems detailed in Czekala et al. (2019) and Ceppi et al. (2024).

5 CONCLUSIONS

Our suite of hydrodynamical simulations shed light on the intricate dynamics of material accretion from circumbinary discs in binary star systems, particularly when considering the binary–disc misalignment. We conducted SPH simulations varying initial tilts from 0° to 180°, encompassing coplanar prograde, polar, and coplanar retrograde alignments. Our findings reveal distinctive accretion patterns contingent upon the initial disc tilt. Discs evolving towards prograde coplanar alignment exhibit alternating preferential accretion on to the primary and secondary stars, while those approaching polar alignment may experience disc breaking and subsequent transition to alternating preferential accretion due to strong disc warping. Conversely, discs undergoing retrograde coplanar alignment do not incite alternating preferential accretion. These results demonstrate the pivotal role of initial disc tilt in shaping accretion rate evolution, which can may be used as a diagnostic discerning binary–disc misalignment.

The results from this work may also be applied to supermassive black hole binaries (SMBHBs) as our simulations are scale free. Since galaxy mergers are expected to channel large amounts of gas toward the centre of the merger remnant (Hopkins et al. 2006), gaseous circumbinary discs should naturally occur around SMBHBs. Measuring the accretion rates of SMBHBs effectively (e.g. D'Orazio, Duffell & Tiede 2024), and showing possible signs of alternating preferential accretion may shed light on the system architecture.

ACKNOWLEDGEMENTS

We thank the anonymous referee for helping to improve the quality of the manuscript. JLS thanks Diego J. Muñoz for helpful suggestions that improved the quality of the manuscript. JLS acknowledges funding from the ASIAA Distinguished Postdoctoral Fellowship and the Taiwan Foundation for the Advancement of Outstanding Scholarship. Y-PL was supported in part by the Natural Science Foundation of China (grants nos. 12373070, and 12192223) and the Natural Science Foundation of Shanghai (grant no. 23ZR1473700).

DATA AVAILABILITY

The data supporting the plots within this article are available on reasonable request to the corresponding author. A public version of the PHANTOM and SPLASH codes are available at https://github.com/danieljprice/phantom and http://users.monash.edu.au/~dprice/splash/download.html, respectively. The 3D renderings made use of PARAVIEW, which is available at https://www.paraview.org/.

REFERENCES

Alcalá J. M. et al., 2014, A&A, 561, A2
Alves F. O., Caselli P., Girart J. M., Segura-Cox D., Franco G. A. P., Schmiedeke A., Zhao B., 2019, Science, 366, 90
Aly H., Lodato G., 2020, MNRAS, 492, 3306
Ansdell M. et al., 2018, ApJ, 859, 21
Artymowicz P., Lubow S. H., 1994, ApJ, 421, 651
Artymowicz P., Lubow S. H., 1996, ApJl, 467, L77
Bate M. R., Bonnell I. A., 1997, MNRAS, 285, 33
Bate M. R., Bonnell I. A., Price N. M., 1995, MNRAS, 277, 362
Bate M. R., Bonnell I. A., Clarke C. J., Lubow S. H., Ogilvie G. I., Pringle J. E., Tout C. A., 2000, MNRAS, 317, 773
Bate M. R., Bonnell I. A., Bromm V., 2002, MNRAS, 336, 705
Bell C. P. M., Mamajek E. E., Naylor T., 2015, MNRAS, 454, 593
Bohn A. J. et al., 2022, A&A, 658, A183
Calvet N., Gullbring E., 1998, ApJ, 509, 802
Calvet N., Muzerolle J., Briceño C., Hernández J., Hartmann L., Saucedo J. L., Gordon K. D., 2004, AJ, 128, 1294
Casassus S. et al., 2015, ApJ, 811, 92
Ceppi S., Cuello N., Lodato G., Clarke C., Toci C., Price D. J., 2022, MNRAS, 514, 906
Ceppi S., Longarini C., Lodato G., Cuello N., Lubow S. H., 2023, MNRAS, 520, 5817
Ceppi S., Cuello N., Lodato G., Longarini C., Price D. J., Elsender D., Bate M. R., 2024, A&A, 682, A104
Cody A. M., Hillenbrand L. A., 2010, ApJS, 191, 389
Corporaal A., Kluska J., Van Winckel H., Bollen D., Kamath D., Min M., 2021, A&A, 650, L13
Cuadra J., Armitage P. J., Alexander R. D., Begelman M. C., 2009, MNRAS, 393, 1423
Cuello N., Giuppone C. A., 2019, A&A, 628, A119
Czekala I., Chiang E., Andrews S. M., Jensen E. L. N., Torres G., Wilner D. J., Stassun K. G., Macintosh B., 2019, ApJ, 883, 22
Czekala I., Ribas Á., Cuello N., Chiang E., Macías E., Duchêne G., Andrews S. M., Espaillat C. C., 2021, ApJ, 912, 6
D'Orazio D. J., Haiman Z., MacFadyen A., 2013, MNRAS, 436, 2997
D'Orazio D. J., Duffell P. C., Tiede C., 2024, ApJ, 977, 244
Deng H., Ogilvie G. I., 2022, MNRAS, 512, 6078
Doğan S., Nixon C., King A., Price D. J., 2015, MNRAS, 449, 1251
Doğan S., Nixon C. J., King A. R., Pringle J. E., 2018, MNRAS, 476, 1519
Drewes N. C., Nixon C. J., 2021, ApJ, 922, 243
Duffell P. C., D'Orazio D., Derdzinski A., Haiman Z., MacFadyen A., Rosen A. L., Zrake J., 2020, ApJ, 901, 25
Duffell P. C. et al., 2024, ApJ, 970, 156
Dunhill A. C., Cuadra J., Dougados C., 2015, MNRAS, 448, 3545
Duquennoy A., Mayor M., 1991, A&A, 248, 485
Facchini S., Juhász A., Lodato G., 2018, MNRAS, 473, 4459
Fairbairn C. W., Ogilvie G. I., 2021, MNRAS, 508, 2426
Farris B. D., Duffell P., MacFadyen A. I., Haiman Z., 2014, ApJ, 783, 134
Franchini A., Lubow S. H., Martin R. G., 2019, ApJ, 880, L18
Franchini A., Sesana A., Dotti M., 2021, MNRAS, 507, 1458
Franchini A., Lupi A., Sesana A., 2022, ApJ, 929, L13
Franchini A., Lupi A., Sesana A., Haiman Z., 2023, MNRAS, 522, 1569
Franchini A., Prato A., Longarini C., Sesana A., 2024, A&A, 688, A174
Gullbring E., Hartmann L., Briceño C., Calvet N., 1998, ApJ, 492, 323
Hanawa T., Ochi Y., Ando K., 2010, ApJ, 708, 485
Hartmann L., Calvet N., Gullbring E., D'Alessio P., 1998, ApJ, 495, 385
Heath R. M., Nixon C. J., 2020, A&A, 641, A64
Hopkins P. F., Hernquist L., Cox T. J., Di Matteo T., Robertson B., Springel V., 2006, ApJS, 163, 1
Hueso R., Guillot T., 2005, A&A, 442, 703
Ingleby L. et al., 2013, ApJ, 767, 112
Jensen E. L. N., Dhital S., Stassun K. G., Patience J., Herbst W., Walter F. M., Simon M., Basri G., 2007, AJ, 134, 241
Kennedy G. M. et al., 2019, Nat. Astron., 3, 230
Kraus S. et al., 2017, ApJ, 835, L5
Kraus S. et al., 2020, Science, 369, 1233

Kurosawa R., Romanova M. M., 2013, MNRAS, 431, 2673
Lai D., Muñoz D. J., 2023, ARA&A, 61, 517
Li D., Zhou J.-L., Zhang H., 2014, MNRAS, 437, 3832
Lodato G., Price D. J., 2010, MNRAS, 405, 1212
Lodato G., Pringle J. E., 2007, MNRAS, 381, 1287
Lubow S. H., Artymowicz P., 2000, in Mannings V., Boss A. P., Russell S. S.eds, Protostars and Planets IV. University of Arizona, Tuscon, p. 731
Lubow S. H., Martin R. G., 2018, MNRAS, 473, 3733
Lubow S. H., Ogilvie G. I., 2000, ApJ, 538, 326
Lubow S. H., Martin R. G., Nixon C., 2015, ApJ, 800, 96
MacFadyen A. I., Milosavljević M., 2008, ApJ, 672, 83
Manara C. F., Robberto M., Da Rio N., Lodato G., Hillenbrand L. A., Stassun K. G., Soderblom D. R., 2012, ApJ, 755, 154
Manara C. F., Fedele D., Herczeg G. J., Teixeira P. S., 2016, A&A, 585, A136
Manara C. F. et al., 2017, A&A, 604, A127
Martin R. G., Lubow S. H., 2017, ApJ, 835, L28
Martin R. G., Lubow S. H., 2019, MNRAS, 490, 1332
Miranda R., Lai D., 2015, MNRAS, 452, 2396
Miranda R., Muñoz D. J., Lai D., 2017, MNRAS, 466, 1170
Muñoz D. J., Lai D., 2016, ApJ, 827, 43
Muñoz D. J., Lithwick Y., 2020, ApJ, 905, 106
Muñoz D. J., Miranda R., Lai D., 2019, ApJ, 871, 84
Muñoz D. J., Lai D., Kratter K., Miranda R., 2020, ApJ, 889, 114
Nealon R., Price D. J., Nixon C. J., 2015, MNRAS, 448, 1526
Nealon R., Ragusa E., Gerosa D., Rosotti G., Barbieri R., 2022, MNRAS, 509, 5608
Nixon C. J., 2012, MNRAS, 423, 2597
Nixon C., King A., Price D., 2013, MNRAS, 434, 1946
Ochi Y., Sugimoto K., Hanawa T., 2005, ApJ, 623, 922
Papaloizou J. C. B., Lin D. N. C., 1995, ApJ, 438, 841
Papaloizou J. C. B., Nelson R. P., Masset F., 2001, A&A, 366, 263
Price D. J. et al., 2018, PASA, 35, e031
Rabago I., Zhu Z., Lubow S., Martin R. G., 2023, MNRAS, 533, 360
Rafikov R. R., 2016, ApJ, 830, 7
Ragusa E., Lodato G., Price D. J., 2016, MNRAS, 460, 1243
Ragusa E., Alexander R., Calcino J., Hirsh K., Price D. J., 2020, MNRAS, 499, 3362
Raj A., Nixon C. J., Doğan S., 2021, ApJ, 909, 81
Rigliaco E., Natta A., Testi L., Randich S., Alcalà J. M., Covino E., Stelzer B., 2012, A&A, 548, A56
Roedig C., Sesana A., Dotti M., Cuadra J., Amaro-Seoane P., Haardt F., 2012, A&A, 545, A127
Shakura N. I., Sunyaev R. A., 1973, A&A, 24, 337
Shi J.-M., Krolik J. H., Lubow S. H., Hawley J. F., 2012, ApJ, 749, 118
Siwek M., Weinberger R., Muñoz D. J., Hernquist L., 2023, MNRAS, 518, 5059
Smallwood J. L., Lubow S. H., Franchini A., Martin R. G., 2019, MNRAS, 486, 2919
Smallwood J. L., Franchini A., Chen C., Becerril E., Lubow S. H., Yang C.-C., Martin R. G., 2020, MNRAS, 494, 487
Smallwood J. L., Nealon R., Chen C., Martin R. G., Bi J., Dong R., Pinte C., 2021a, MNRAS, 508, 392
Smallwood J. L., Martin R. G., Lubow S. H., 2021b, ApJ, 907, L14
Smallwood J. L., Lubow S. H., Martin R. G., 2022, MNRAS, 514, 1249
Smallwood J. L., Martin R. G., Lubow S. H., 2023, MNRAS, 520, 2952
Stassun K. G., Torres G., Kounkel M., Feliz D. L., Bouma L. G., Howell S. B., Gnilka C. L., Furlan E., 2022, ApJ, 941, 125
Thun D., Kley W., Picogna G., 2017, A&A, 604, A102
Tiede C., Zrake J., MacFadyen A., Haiman Z., 2020, ApJ, 900, 43
Tofflemire B. M., Mathieu R. D., Johns-Krull C. M., 2019, AJ, 158, 245
Valenti J. A., Basri G., Johns C. M., 1993, AJ, 106, 2024
Venuti L. et al., 2014, A&A, 570, A82
Vernet J. et al., 2011, A&A, 536, A105
White R. J., Ghez A. M., 2001, ApJ, 556, 265
Young A. K., Stevenson S., Nixon C. J., Rice K., 2023, MNRAS, 525, 2616
Zhu Z., 2019, MNRAS, 483, 4221

This paper has been typeset from a TEX/LATEX file prepared by the author.